Hard gap in epitaxial semiconductorsuperconductor nanowires

W. Chang^{1,2}, S. M. Albrecht¹, T. S. Jespersen¹, F. Kuemmeth¹, P. Krogstrup¹, J. Nygård¹ and C. M. Marcus¹*

Many present and future applications of superconductivity would benefit from electrostatic control of carrier density and tunnelling rates, the hallmark of semiconductor devices. One particularly exciting application is the realization of topological superconductivity¹ as a basis for quantum information processing^{2,3}. Proposals in this direction based on the proximity effect in semiconductor nanowires are appealing because the key ingredients are currently in hand^{4,5}. However, previous instances of proximitized semiconductors show significant tunnelling conductance below the superconducting gap, suggesting a continuum of subgap states—a situation that nullifies topological protection^{6,7}. Here, we report a hard superconducting gap induced by the proximity effect in a semiconductor, using epitaxial InAs-Al semiconductor-superconductor nanowires. The hard gap, together with favourable material properties and gate-tunability, makes this new hybrid system attractive for a number of applications, as well as fundamental studies of mesoscopic superconductivity.

Key signatures of topological superconductivity, including a characteristic zero-bias tunnelling peak appearing at finite magnetic field, have been reported by several groups over the past few years^{8–11}. In all cases, a soft gap is also seen, indicated by sizable subgap conductance. The origin of the soft gap is not fully understood, with recent theory attributing it to disorder at the semiconductor/superconductor interface¹². Besides complicating an already complex mesoscopic system by allowing alternative (Kondo) processes that themselves can give rise to zero-bias tunnelling peaks, subgap states are fatal to topological protection. This is because quasiparticles occupying subgap states will inadvertently participate in braiding, thus influencing the resulting quantum states in an unpredictable and possibly time-dependent way^{6,7}.

Here, InAs nanowires were grown in the wurzite [0001] direction by molecular beam epitaxy (MBE) using gold nanoparticles as catalysts¹³. Once the nanowires reached a length of 5–10 μm, Al was grown at a low temperature by angled deposition within the MBE chamber. The resulting semiconductor/superconductor interface, shown in Fig. 1c, appears coherent, domain-matched and impurity free. The material growth is described in detail in ref. 14. Rotating the substrate during Al growth results in full-shell nanowires with epitaxial interfaces on all facets (Fig. 1a), while directional growth without rotating yields half-shell nanowires, with epitaxial Al on two or three facets of the hexagonal InAs core (Fig. 5a). The nanowires were dispersed onto a doped Si substrate with a 100 nm oxide. The Al shell was contacted by superconducting Ti/Al (5/130 nm) and the InAs core (exposed with a selective Al etch) by normal Ti/Au (5/80 nm). Modest in situ ion milling was used to improve contact between both the core and shell to leads. A device similar to the one measured is shown in Fig. 1d. Control devices were fabricated by etching away the Al shell and evaporating Ti/Al in selected areas (Fig. 1b,d). (The 5 nm Ti sticking layer improved gap hardness in all control devices; see Supplementary Section 2.)

Measurements were carried out in a dilution refrigerator with a base temperature of 20 mK. The carrier density in the exposed InAs was tuned via the backgate voltage $V_{\rm BG}$ (the side gate was not used in these measurements). The external magnetic field B was applied along the nanowire axis, unless stated otherwise. Seven epitaxial devices (as well as eight control devices) have been measured to date and show similar behaviour.

Tunnelling spectra of a full-shell epitaxial device and an evaporated control device in the weak tunnelling regime, with conductance

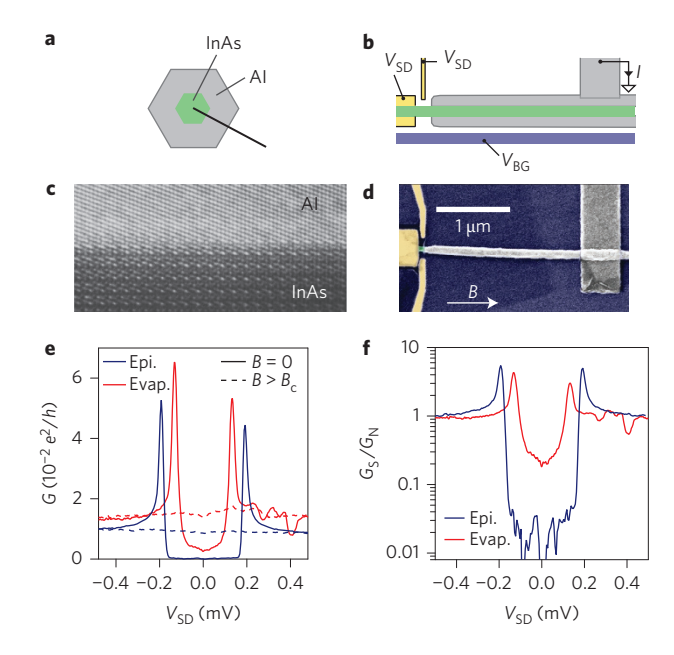


Figure 1 | Epitaxial full-shell device and hard induced gap. a, Schematic cross-section of epitaxial full-shell nanowire with lnAs core (green) and Al shell (grey). **b**, Measurement set-up, showing Ti/Au leads (yellow), lnAs nanowire (green) and Al shell (grey). **c**, Transmission electron micrograph of epitaxial N/S interface along the cut in **a. d**, Scanning electron micrograph of lithographically similar device (false colour). **e**, Differential conductance as a function of source–drain voltage of an epitaxial full-shell device (blue) and an evaporated control device (red) at B = 0 (solid line) and above the critical field $B > B_c$ (dashed line). **f**, Normalized differential conductance. Epitaxial full-shell nanowires exhibit subgap conductance suppression by a factor of ≈ 100

¹Center for Quantum Devices, Niels Bohr Institute, University of Copenhagen, Universitetsparken 5, 2100 Copenhagen, Denmark. ²Department of Physics, Harvard University, Cambridge, Massachusetts 02138, USA. *e-mail: marcus@nbi.dk

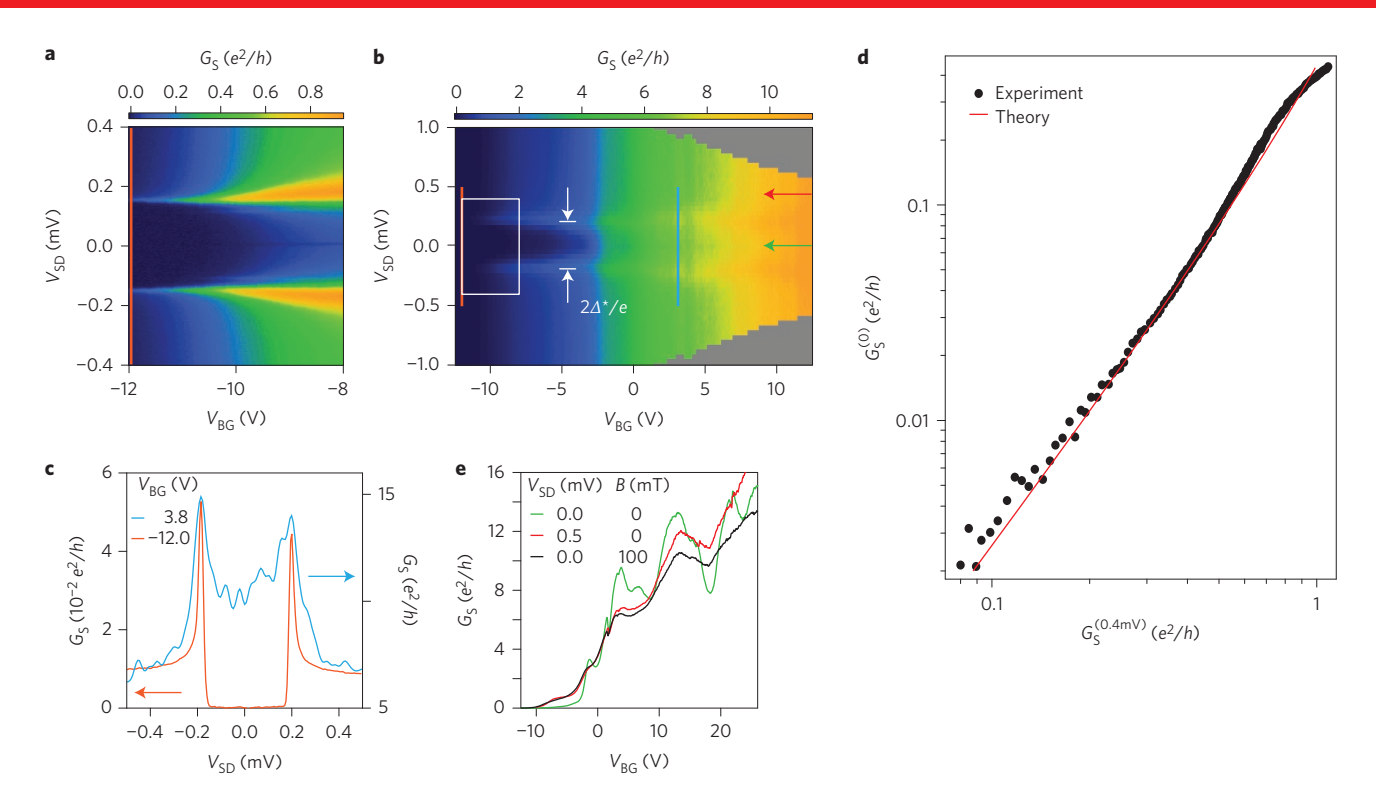


Figure 2 | Gate dependence of conductance of full-shell device. a,b, Differential conductance G_S of a full-shell device as a function of backgate voltage V_{BG} and source-drain voltage V_{SD} . The region in **a** is indicated as a white rectangle in **b**. Red and green arrows in **b** are the cuts in **e**. **c**, Vertical cuts of **a** and **b** in the tunnelling (orange) and high-conductance (blue) regimes. **d**, Zero-bias conductance G_S as a function of high-bias conductance, measured at $V_{SD} = 0.4$ mV (black circles), together with theory of G_S as a function of G_S in the following point of G_S as a function of G_S and G_S are conductance G_S as a function of G_S as a function of G_S as a function of G_S and G_S are conductance G_S and G_S are conductance G_S and G_S are conductance G_S as a function of G_S and G_S are conductance G_S and G_S are conductance

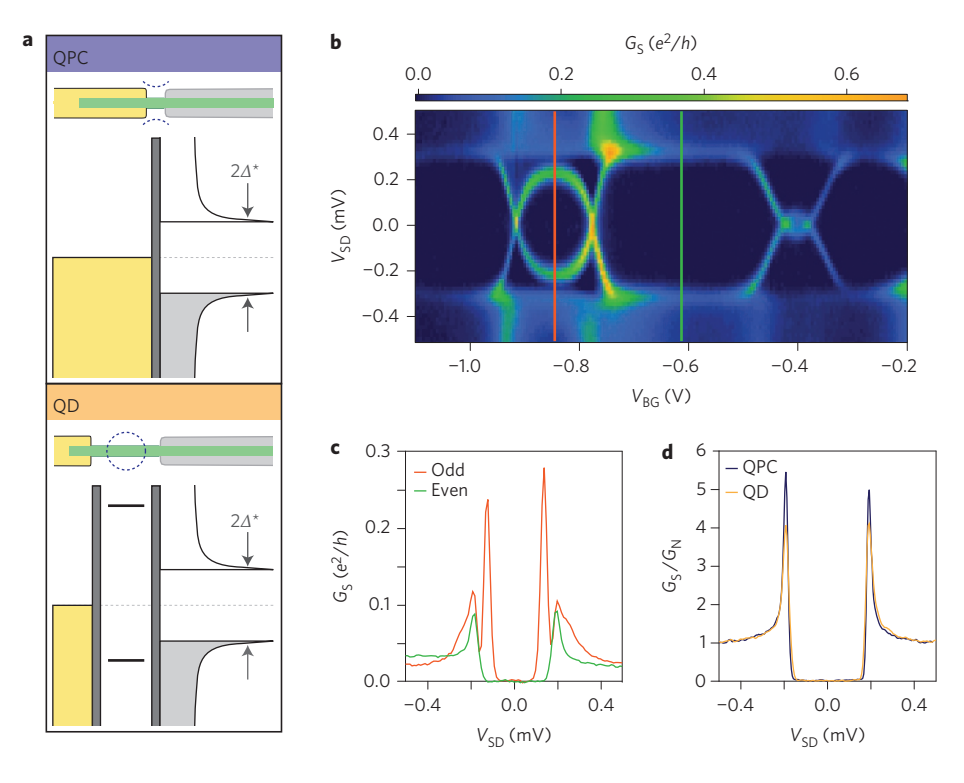


Figure 3 | Comparing quantum point contact and quantum dot devices. a, Schematic of tunnelling from normal metal lead to proximitized wire via a quantum point contact (QPC) barrier (upper) and quantum dot (QD) barrier (lower). b, Andreev bound states in a quantum dot appear as subgap conductance features. Cuts through a Coulomb valley with odd (orange) and even (green) occupancy. c, Tunnelling spectra along cuts in b. d, Comparison of tunnelling measurements of QPC and QD devices in an even valley.

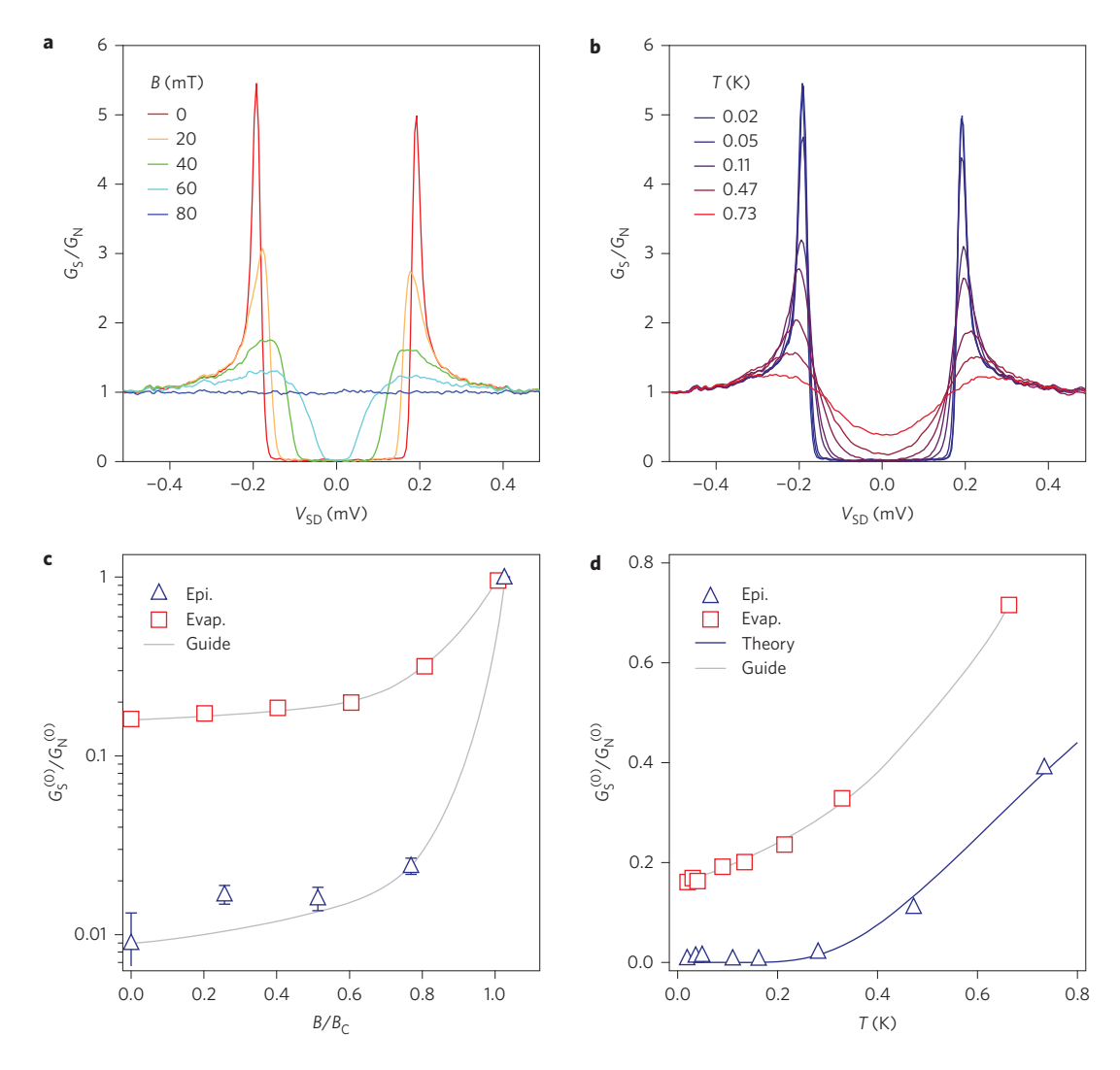


Figure 4 | Magnetic field and temperature dependence of induced gaps. a, Magnetic field dependence of full-shell device. b, Temperature dependence of full-shell device. c,d, Normalized zero-bias conductances of epitaxial device (blue triangles) and evaporated (control) device (red squares). Error bars reflect measurement noise. Blue line in d is a fit to theory, equation (2), with one fit parameter (see main text).

of the exposed core tuned to $G \ll G_0 = 2~e^2/h$, are shown in Fig. 1e. In the superconducting state (B=0), differential conductance $G_{\rm S}$ as a function of source–drain voltage $V_{\rm SD}$ showed strongly suppressed conductance between symmetric peaks. Above a critical value of field, $B_{\rm c}$ (~75 mT for the epitaxial device, ~250 mT for the control), both devices showed a featureless normal-state tunnelling conductances $G_{\rm N}$ of ~0.01 e^2/h . Ratios $G_{\rm S}/G_{\rm N}$ for the epitaxial and control devices are shown in Fig. 1f. The positions of the peaks in $G_{\rm S}$ indicate an induced gap of $\Delta^*=190~{\rm \mu eV}$, similar to the gap of bulk Al. Figure 1f shows the subgap conductance suppressed by a factor of ~100 relative to either the normal state $(B>B_{\rm c})$ or above-gap conductance. The evaporated control device shows a slightly smaller induced gap of 140 ${\rm \mu eV}$ and a suppression of subgap conduction by a factor up to ~5, comparable to previous measurements in proximitized InAs and InSb nanowires^{8-11,15,16}.

Increasing $V_{\rm BG}$ in the full-shell device increased both the subgap and above-gap conductance (Fig. 2). Conductance peaks at $V_{\rm SD}$ = 190 μ V, indicating the induced gap, did not depend on gate voltage. At positive gate voltages (more open barrier), subgap conductance exceeds the corresponding normal state conductance, as expected for a moderate-transmission barrier^{17,18}. Enhanced subgap conductance is evident in Fig. 2c, which shows two vertical cuts taken at low and high backgate voltages (orange and blue lines in Fig. 2a,b). In Fig. 2d, the superconducting zero-bias

conductance is plotted as a function of above-gap conductance ($V_{\rm SD}=0.4~{\rm mV}$), together with a theoretical dependence of $G_{\rm S}(V_{\rm SD}=0)$ on $G_{\rm N}(V_{\rm SD}=0)^{17}$

$$G_{\rm S}|_{V_{\rm SD}=0} = 2G_0 \frac{G_{\rm N}^2}{(2G_0 - G_{\rm N})^2}$$
 (1)

with no fit parameters. Using the high-bias conductance $(V_{\rm SD}=0.4~{\rm mV}>\Delta^*/e)$ in place of the normal state conductance is justified by their observed equality in the experiment (Fig. 1f). Agreement between experiment and the one-channel limit of theory 17 over a broad range of conductances indicates that transmission in the constriction is single channel.

The device reported in Fig. 2 exhibited conductance steps as a function of $V_{\rm BG}$ (Fig. 2e), a typical signature of quantum point contacts (QPCs). Zero-bias conductance in the normal state (black line) shows plateaux at values close to 1, 3, 6 and $10 \, e^2/h$. These unconventional quantization values could be attributed to imperfect transmission of one-dimensional conduction modes¹⁹ or symmetries in the transverse confining potential of the nanowire²⁰. In addition, although we have subtracted line resistances from our measurement set-up, we cannot independently determine contact resistances within the device, which affect plateau values. In the superconducting state and at a source–drain bias above Δ^*/e (red line), the device

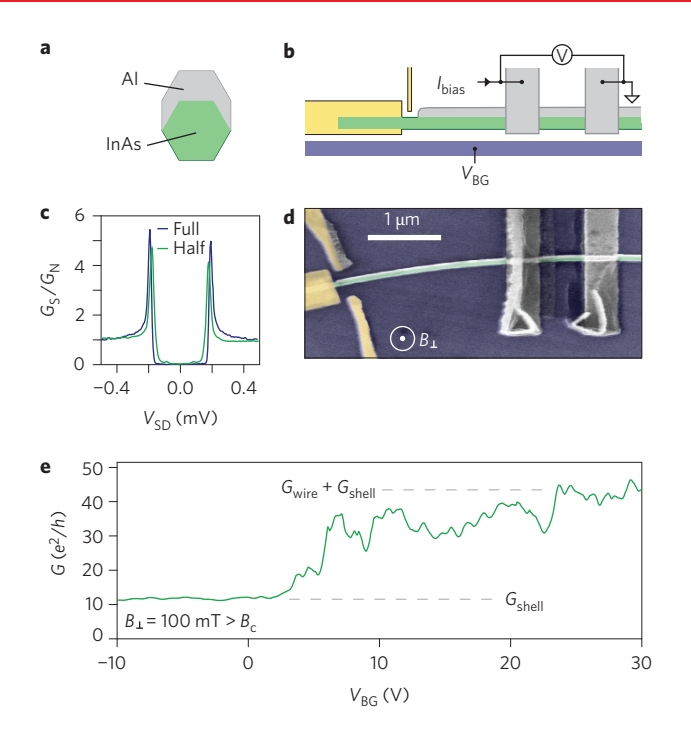


Figure 5 | Epitaxial half-shell device and gate-tunability of InAs core.

- **a**, Cross-section illustration of a half-shell nanowire. **b**, Gate-tunability measurement schematic of a half-shell nanowire device. **c**, Comparison of induced gap quality between an epitaxial full-shell and half-shell device.
- d, Scanning electron micrograph of a lithographically similar device.
- **e**, Conductance of the Al shell and InAs core as a function of $V_{\rm BG}$. Saturating conductance at negative gate voltage suggests wire is depleted in this regime, with all conductance in this regime due to the shell and contact resistance.

conductance shows a similar behaviour, but begins to deviate above $6\,e^2/h$. Plateaux are less well defined at zero bias in the superconducting state (green line). Instead, conductance oscillates around the normal state values and peaks on the lower $V_{\rm BG}$ edge of the normal state plateaux.

In some devices, both epitaxial and evaporated, the exposed core region forms a quantum dot rather than a QPC (Fig. 3a). The formation of a quantum dot instead of a QPC barrier depends on the length of the exposed wire, as indicated in Fig. 3a, but is not yet under full experimental control. In the normal state of an epitaxial full-shell device with a quantum dot barrier, Coulomb blockade diamonds and Kondo-related evenodd structures can be identified (see Supplementary Section 4). Because the charging energy of the reported quantum dot device is larger than the induced gap Δ^* , when V_{BG} is tuned to the middle of an even Coulomb diamond, the discrete quantum dot states are far from the edge of the induced gap. The quantum dot thus acts as a single tunnel barrier between the normal lead and the proximitized InAs core. Accordingly, tunnelling spectra for QPC and even-valley quantum dot devices were found to be essentially identical (Fig. 3d).

In odd-occupied Coulomb valleys, symmetric subgap resonances (SGRs) were observed, forming a characteristic eye shape (Fig. 3b). These SGRs, arising from Andreev bound states or Yu–Shiba–Rusinov states^{21–24}, crossed due to Coulomb interaction, have previously been investigated both experimentally and theoretically^{15,25–31}. Similar quantum dot structures and their associated SGRs in the superconducting state are also observed in the evaporated-Al control devices. Vertical cuts at the particle–hole symmetry point of an odd (orange) and even (green) Coulomb valley are shown in Fig. 3c.

Figure 4 shows the evolution of the proximity-induced gap as a function of magnetic field and temperature. Figure 4c,d compares the normalized zero-bias conductance of an epitaxial full-shell device against an evaporated control device. Because the subgap conductance in epitaxial devices is close to our experimental noise floor, we average over a 40 μV window centred about zero bias and define this value as $G_{\rm S}^{(0)}/G_{\rm N}^{(0)}$. For better comparison, we normalize the applied magnetic field by the critical fields of each device in Fig. 4c. Figure 4d presents the normalized zero-bias conductance as a function of temperature. The temperature dependence of the tunnelling conductance of a N–S junction is given by the expression 32

$$\frac{G_{\rm S}}{G_{\rm N}}|_{V_{\rm SD}=0} = \sqrt{\frac{2\pi\Delta^{*}}{k_{\rm B}T}} e^{-\Delta^{*}/k_{\rm B}T}$$
 (2)

where $k_{\rm B}$ is the Boltzmann constant and T is the temperature. From the theoretical fit, we extract an induced gap of 160 μ eV, close to, but not identical to, the 190 μ eV measured directly from tunnelling spectroscopy. We note in Fig. 4a,c that the floor of the induced gap in the epitaxial devices remains close to zero conductance, rising sharply only when B approaches $B_{\rm c}$. Retaining a hard gap at finite magnetic fields is important for potential applications in topological quantum computing. We do not know of a theoretical treatment of this dependence with which we can compare the data.

Devices with half-shell nanowires were fabricated by identical methods, although with two superconducting Al leads instead of one, both leads contacting the Al half-shell and the InAs core on the uncovered side of the nanowire (Fig. 5). Tunnelling spectroscopy on these devices also shows very low subgap conductance and a gap of 180 μeV (Fig. 5c), slightly smaller than the induced gap in the full-shell devices. The subgap conductance is a factor of ~ 50 below the normal state or high-bias conductance, significantly better than in the evaporated control devices, but not quite as low as the full-shell device, for reasons that are not yet understood.

The use of two superconducting leads in the half-shell device allowed us to measure the conductance of the nanowire while the electron density in the half-exposed InAs core was tuned via a side or backgate. As illustrated in Fig. 5b, conductance across the two Al leads was measured in a current-biased configuration with the device in the normal state $(B_{\perp}=100 \text{ mT} > B_c)$. The conductance remained roughly constant at $\sim 10e^2/h$ below $V_{\rm BG} \approx 3$ V, then rose to \sim 45 e^2/h at more positive $V_{\rm BG}$ (Fig. 5e). We interpret the saturated conductance at negative gate voltages to be the conductance of the Al shell, and the subsequent increase in conductance at positive gate voltages as due to a parallel conduction channel through the InAs core. Using the capacitance model from ref. 33, we estimate the following transport parameters for the InAs core: carrier density (at high V_{BG}) of $n = 5 \times 10^{18} \text{ cm}^{-3}$, mobility of $\mu = 3,300 \text{ cm}^2 \text{ V}^{-1} \text{ s}^{-1}$ and elastic scattering length of $l_e = 100$ nm. These are typical values for InAs nanowires, as reported in refs 34 and 35. However, the expected resistance for our Al shell should be on the order of 10 Ω . The higher measured resistance could be attributed to additional contact resistance between the Al leads and the Al shell, or disorder in the Al shell for this particular sample. Regardless of the series resistance, the observed saturation of conductance at the negative end of the gate voltage range suggests that the wire is fully depleted at that point. Future experiments with multiple side gates will improve control of the density along the wire.

Although the full-shell nanowires provide a fully protective coating as well as an interesting geometry (a cylindrical superconductor) it is presumably the half-shell devices that are of more direct applicability to topological superconductivity and Majorana devices. The possibility of controlling the subband occupation in a large spin–orbit, large *g*-factor, quasi-one-dimensional semiconductor, while maintaining a hard induced superconducting gap, makes

the epitaxial half-shell nanowire an ideal platform for nanowire-based Majorana devices and many other applications.

Received 31 August 2014; accepted 18 November 2014; published online 12 January 2015

References

- Kitaev, A. Y. Unpaired Majorana fermions in quantum wires. *Phys. Usp.* 44, 131–136 (2001).
- Nayak, C., Simon, S. H., Stern, A., Freedman, M. & Das Sarma, S. Non Abelian anyons and topological quantum computation. *Rev. Mod. Phys.* 80, 1083–1159 (2008).
- Alicea, J., Oreg, Y., Refael, G., von Oppen, F. & Fisher, M. P. A. Non-Abelian statistics and topological quantum information processing in 1D wire networks. *Nature Phys.* 7, 412–417 (2011).
- Lutchyn, R. M., Sau, J. D. & Das Sarma, S. Majorana fermions and a topological phase transition in semiconductor–superconductor heterostructures. *Phys. Rev. Lett.* 105, 077001 (2010).
- Oreg, Y., Refael, G. & von Oppen, F. Helical liquids and Majorana bound states in quantum wires. *Phys. Rev. Lett.* 105, 177002 (2010).
- Cheng, M., Lutchyn, R. M. & Das Sarma, S. Topological protection of Majorana qubits. *Phys. Rev. B* 85, 165124 (2012).
- Rainis, D. & Loss, D. Majorana qubit decoherence by quasiparticle poisoning. Phys. Rev. B 85, 174533 (2012).
- Mourik, V. et al. Signatures of Majorana fermions in hybrid superconductorsemiconductor nanowire devices. Science 336, 1003–1007 (2012).
- Das, A. et al. Zero-bias peaks and splitting in an Al-InAs nanowire topological superconductor as a signature of Majorana fermions. Nature Phys. 8, 887–895 (2012).
- Deng, M. T. et al. Anomalous zero-bias conductance peak in a Nb-InSb nanowire-Nb hybrid device. Nano Lett. 12, 6414-6419 (2012).
- Churchill, H. O. H. et al. Superconductor-nanowire devices from tunneling to the multichannel regime: Zero-bias oscillations and magnetoconductance crossover. Phys. Rev. B 87, 241401 (2013).
- Takei, S., Fregoso, B. M., Hui, H-Y., Lobos, A. M. & Das Sarma, S. Soft superconducting gap in semiconductor Majorana nanowires. *Phys. Rev. Lett.* 110, 186803 (2013).
- Krogstrup, P. et al. Junctions in axial III-V heterostructure nanowires obtained via an interchange of group III elements. Nano Lett. 9, 3689–3693 (2009).
- Krogstrup, P. et al. Epitaxy of semiconductor-superconductor nanowires. Nature Mater. http://dx.doi.org/10.1038/nmat4176 (2015).
- Chang, W., Manucharyan, V. E., Jespersen, T. S., Nygård, J. & Marcus, C. M. Tunneling spectroscopy of quasiparticle bound states in a spinful Josephson junction. *Phys. Rev. Lett.* 110, 217005 (2013).
- Finck, A. D. K., Van Harlingen, D. J., Mohseni, P. K., Jung, K. & Li, X. Anomalous modulation of a zero-bias peak in a hybrid nanowire– superconductor device. *Phys. Rev. Lett.* 110, 126406 (2013).
- Beenakker, C. W. J. Quantum transport in semiconductor–superconductor microjunctions. *Phys. Rev. B* 46, 12841–12844 (1992).
- Blonder, G. E., Tinkham, M. & Klapwijk, T. M. Transition from metallic to tunneling regimes in superconducting microconstrictions: Excess current, charge imbalance, and supercurrent conversion. *Phys. Rev. B* 25, 4515–4532 (1982).
- 19. Chuang, S. et al. Ballistic InAs nanowire transistors. Nano Lett. 13, 555–558 (2013).

- Ford, A. C., Kumar, S. B., Kapadia, R., Guo, J. & Javey, A. Observation of degenerate one-dimensional sub-bands in cylindrical InAs nanowires. *Nano Lett.* 12, 1340–1343 (2012).
- Yu, L. Bound state in superconductors with paramagnetic impurities. Acta Phys. Sin. 21, 75–91 (1965).
- Shiba, H. Classical spins in superconductors. Prog. Theor. Phys. 40, 435–451 (1968).
- Rusinov, A. I. Theory of gapless superconductivity in alloys containing paramagnetic impurities. Sov. Phys. JETP 29, 1101–1106 (1969).
- Koerting, V., Andersen, B. M., Flensberg, K. & Paaske, J. Nonequilibrium transport via spin-induced subgap states in superconductor/quantum dot/normal metal cotunnel junctions. *Phys Rev. B* 82, 2451081–2451084 (2010).
- Deacon, R. S. et al. Tunneling spectroscopy of Andreev energy levels in a quantum dot coupled to a superconductor. Phys. Rev. Lett. 104, 076805 (2010).
- Lee, E. J. H. et al. Spin-resolved Andreev levels and parity crossings in hybrid superconductor–semiconductor nanostructures. Nature Nanotech. 9, 79–84 (2014).
- Dirks, T. et al. Transport through Andreev bound states in a graphene quantum dot. Nature Phys. 7, 386–390 (2011).
- Pillet, J-D. et al. Andreev bound states in supercurrent-carrying carbon nanotubes revealed. Nature Phys. 6, 965–969 (2010).
- Meng, T., Florens, S. & Simon, P. Self-consistent description of Andreev bound states in Josephson quantum dot devices. *Phys. Rev. B* 79, 224521 (2009).
- Deacon, R. S. et al. Kondo-enhanced andreev transport in single selfassembled InAs quantum dots contacted with normal and superconducting leads. Phys. Rev. B 81, 121308 (2010).
- 31. Vecino, E., Martín-Rodero, A. & Yeyati, A. L. Josephson current through a correlated quantum level: Andreev states and π junction behavior. *Phys. Rev. B* **68**, 035105 (2003).
- 32. Tinkham, M. Introduction to Superconductivity 2nd edn (Dover, 2004).
- Wunnicke, O. Gate capacitance of back-gated nanowire field-effect transistors. Appl. Phys. Lett. 89, 083102 (2006).
- Doh, Y-J. et al. Tunable supercurrent through semiconductor nanowires. Science 309, 272–275 (2005).
- Jespersen, T. S., Polianski, M. L., Sørensen, C. B., Flensberg, K. & Nygård, J. Mesoscopic conductance fluctuations in InAs nanowire-based SNS junctions. New J. Phys. 11, 113025 (2009).

Acknowledgements

The authors thank E. Johnson for assistance with electron microscopy and K. Flensberg for discussions. This research was supported by Microsoft Project Q, the Danish National Research Foundation, the Carlsberg Foundation, the Villum Foundation, the Lundbeck Foundation and the European Commission.

Author contributions

P.K., T.S.J. and J.N. developed the nanowire materials. W.C. and S.A. fabricated the devices and carried out the measurements with input from F.K., T.S.J. and C.M. All authors contributed to analysing and interpreting the data and to writing the manuscript.

Additional information

Supplementary information is available in the online version of the paper. Reprints and permissions information is available online at www.nature.com/reprints. Correspondence and requests for materials should be addressed to C.M.M.

Competing financial interests

The authors declare no competing financial interests.